Technical

Report

Quarterly Progress Report
Q-C1880-3

INVESTIGATION OF THE DEFORMATION OF BERYLLIUM SINGLE CRYSTALS UNDER HIGH PRESSURE

THE FRANKLIN INSTITUTE RESEARCH LABORATORIES
BENJAMIN FRANKLIN PARKWAY • PHILADELPHIA, PENNA. 19103

Technical

Quarterly Progress Report
Q-C1880-3

Report

INVESTIGATION OF THE DEFORMATION OF BERYLLIUM SINGLE CRYSTALS UNDER HIGH PRESSURE

by

V. Damiano
J. Hanafee
N. Inoue
G. London
H. Conrad

December 1, 1966 to February 28, 1967

Prepared for

AIR FORCE MATERIALS LABORATORY
Wright-Patterson Air Force Base, Ohio 45433

Contract No. AF 33(615)-5193

THE FRANKLIN INSTITUTE RESEARCH LABORATORIES
BENJAMIN FRANKLIN PARKWAY • PHILADELPHIA, PENNA. 19103

ABSTRACT

This progress report describes continued c-axis compression testing of ingot and zone leveled beryllium crystals under hydrostatic pressures in the range 145 to 293 ksi. Ductile behavior with active non-basal slip activity commenced, with this purity material in the range 250 to 300 ksi. Optical examination and electron transmission microscopy confirmed the occurrence of $\{11\bar{2}2\}$ slip.

Continued equipment design and construction and c-axis specimen preparation is also summarized.

TABLE OF CONTENTS

LIST OF FIGURES

LIST OF FIGURES (Concl.)

LIST OF TABLES

INTRODUCTION

This is the third quarterly progress report on a program of study of the effect of hydrostatic pressure on the deformation behavior of beryllium single crystals tested in c-axis compression. Two levels of material purity are included in the study program.

Progress this quarter has included continued c-axis compression testing of both ingot purity and zone leveled (low purity) single crystal specimens to a maximum hydrostatic pressure of 293 ksi at room temperature. Optical and electron microscope examination of the tested crystals indicate that substantial pyramidal deformation occurs in the pressure range 250 to 300 ksi. These observations are described in detail in the body of this report. Progress has also continued in the design and construction of the FIRL constant pressure test apparatus. The preparation of oriented and electropolished c-axis compression test specimens has also continued during this quarter.

HYDROSTATIC PRESSURE EQUIPMENT

A sub-press assembly for aligned, axial loading of the c-axis compression specimens was completed during the early part of this quarter. This assembly was used to conduct four c-axis compression tests over the hydrostatic pressure range 145 ksi to 293 ksi. All these tests were successful in that the high stresses at fracture indicated that true axial loading (or very nearly so) had been accomplished.

A detailed design of the high pressure vessel for this FIRL High Pressure test assembly has been prepared and the vessel itself has been substantially completed. This pressure vessel is shown in Figure 1. This figure supplements and completes Figure 2 of Q-C1880-1.

There are two main features of the design of this pressure system:

1) Since the specimen is to be strained at constant hydrostatic pressure, the pressurizing system and the specimen loading systems are completely independent of one another. In the system shown in Figure 1, hydrostatic pressure will be produced by motion of the top and bottom pistons, while compression of the test specimen will be achieved by motion of the container.

2) A hydrostatic pressure of 400 ksi is to be attained using a liquid medium. The maximum container pressure in a piston-cylinder type apparatus is about 170 ksi at which point the material of the bore surface is at its yield stress. The design figure of 170 ksi is based on a 300 ksi yield stress for maraging steel and a maximum distortion energy failure criterion. Taupel* has shown this failure criterion to be in good agreement with experimental data. Consequently, either a two-stage compression device or some means of pre-stressing the pressure bearing cylinder is needed to attain pressure values higher than the 170 ksi figure. In the present design, the maximum pressure of 400 ksi is attained by a two-stage compression with the maximum container pressure of about 200 ksi per stage.

The c-axis compression test will be carried out essentially as described previously (Q-C1880-1). The design allows that at full pressurization the top piston will not yet contact the test specimen. At this time raising the container will effect the compression test. Any pressure variations occurring during the test may be corrected using the 100 ton ram actuator.

*J. H. Taupel, "Yield and Bursting Characteristics of Heavy Walled Cylinders," Trans. ASME, July 1956.

CRYSTAL PREPARATION

Eleven c-axis compression specimens of the zone leveled material (SR-11) have been given final orientation, lapping and electropolishing and are available for testing. Present plans are to test five of these in the Harwood apparatus and five in the FIRL equipment. The 11th crystal will be tested at ambient pressure in the existing c-axis compression test apparatus.

About 20 specimen blanks have been spark machined from the high purity 12 zone pass material, designated SR-3. Eleven of these specimen blanks are in the process of final orientation, lapping and electropolishing and will be tested with the same breakdown as the SR-11 material.

TEST RESULTS

Four c-axis compression tests were conducted this quarter, three on ingot S.R. material (designated ISR) and the fourth on zone leveled SR-11 material. The tests were conducted using the axial loading subpress constructed for the Bridgman-Birch type 30 kilobar apparatus at FIRL (mfg. by the Harwood Engineering Co.).

Load was measured on an internal load cell consisting of four foil gages mounted on a load bearing member in full bridge configuration. The load cell operated entirely within the pressure chamber and directly sensed the load applied to the specimen. Calibration of this load cell with a proving ring was carried out in the pressure chamber at ambient pressure before and after the pressure tests. Calibration after the tests showed that the load cell was within 1% of the original calibration.

Compression testing is accomplished by loading with the high pressure piston. The chamber pressure increases continuously during the compression test. Table I shows the loading pressure range and the stress at fracture for the crystals tested. Note the very high stress at fracture measured for specimen ISR-12 at the highest hydrostatic pressure. Substantial ductility was indicated for this crystal test as will be described below.

Table I

SUMMARY OF SINGLE CRYSTAL C-AXIS COMPRESSION TESTS UNDER HYDROSTATIC PRESSURE

Spec.	Pressure Range P_i* ksi	P_f** ksi	Fracture Stress ksi	Observed Behavior
ISR-10	145.8	168.1	299.0	Brittle
ISR-11	238.0	255.0	297.0	Brittle
ISR-12	261.0	293.0	438.0	Ductile
SR-11-1	156.0	164.0	331.0	Brittle

*P_i = pressure at onset of loading.

**P_f = pressure at crystal failure.

STRUCTURAL CHARACTERIZATION

The structural characterization of all crystals tested by c-axis compression under hydrostatic pressure consisted of:

(1) The macrophotography of at least two mutually perpendicular lateral surfaces of the tested crystal at a magnification of 15X.

(2) Optical microscopy of the lateral surfaces to determine the active slip or twinning modes which operated.

(3) Electron transmission microscopy studies of at least one foil cut from the bulk crystals.

1. SR Ingot Crystals

a. Specimen ISR-10 (146-168 ksi Pressure)

A macroscopic photograph showing two mutually perpendicular lateral surfaces parallel to the $(\bar{1}010)$ and $(11\bar{2}0)$ planes after compression to failure under hydrostatic pressure is shown in Figure 2(a) and (b) respectively. Failure appears to have occurred by shearing on a non-crystallographic plane which was nearly parallel to the $(10\bar{1}2)$ traces seen at T on the $(11\bar{2}0)$ surface. Basal slip lines and $(10\bar{1}2)$ twin traces were quite prominent as seen in the optical photomicrographs in Figures 3 and 4.

Unusual rectangular markings as seen at S were frequently observed on the lateral surfaces. In some cases the markings appeared to be associated with twins as in Figure 4 but they also frequently appeared in regions free of twins as in Figure 3. Interferrometric studies revealed that the rectangularly shaped regions were actually extrusions and were very likely the result of slip on closely spaced basal and $(\bar{1}010)$ prism planes.

Localized regions of intense basal and prism slip were commonly observed as seen in Figure 5. It should be noted that such markings were not observed for c-axis compression at ambient pressure and are believed to be associated with the hydrostatic high pressure environment.

There was no evidence of profuse pyramidal slip; however, some evidence of slip lines which were inclined to the (0001) traces were observed, for example, at G in Figure 5 and at the fracture in Figure 6 which is near the region F in Figure 2. These closely matched a $\{11\bar{2}2\}$ trace for this surface. $(10\bar{1}0)$ traces were also seen in these regions. Although a single set of slip traces observed on one surface is generally insufficient evidence to make a positive identification, it is strongly felt from prior experience that slip on the $\{11\bar{2}2\}$ type plane had occurred in a very localized region near the fracture.

Electron transmission microscopy studies of a foil cut parallel to the $\{11\bar{2}0\}$ surface of this specimen did not reveal the presence of dislocations having non-basal Burgers vectors. The dark field contrast obtained for g.(0002) and g.($\bar{1}010$) of the same region are shown in Figure 7(a) and (b). Numerous dislocations and dislocation loops having Burgers vectors coincident with the basal plane appear in contrast in (b) and are extinguished for g.(0002) in (a).

b. Specimen ISR-11 (238-255 ksi Pressure)

A macroscopic photograph showing the two mutually perpendicular lateral surfaces parallel to the $(11\bar{2}0)$ and $(10\bar{1}0)$ planes is shown in Figure 8. The fracture in this case was somewhat different from that previously described. The fracture appeared in the region of the platens and the fracture plane was inclined at a different angle to the (0001) plane than that observed for specimen ISR-10.

Optical microscopy examination of the lateral surfaces revealed markings which were similar to those in Figures 3 and 4. One set of pyramidal slip lines were observed only in the vicinity of the fracture, similar to those shown in Figure 6. Electron transmission microscopy studies of a foil cut parallel to the $\{11\bar{2}0\}$ surface did not reveal the presence of dislocations having non-basal Burgers vectors. The contrast effects obtained for g.(0002) and g.($\bar{1}010$) for the same area are shown in Figure 9(a) and (b). Dislocations having Burgers vectors lying in the basal plane $1/3 \langle 11\bar{2}0 \rangle$ type are revealed for the operating g.($\bar{1}010$) in Figure 8(b). These are extinguished for g.(0002) Figure 8(a).

c. Specimen ISR-12 (261-293 ksi Pressure)

The macroscopic photographs showing the two mutually perpendicular lateral surfaces parallel to the $(11\bar{2}0)$ and $(\bar{1}010)$ planes are shown in Figure 10. The fracture surface was again non-crystallographic and appeared in the region of the platens similar to specimen ISR-11.

Optical microscopy of the lateral surfaces revealed *profuse pyramidal* slip lines on both the $(11\bar{2}0)$ face and the $(\bar{1}010)$ face. The slip traces observed on the $(\bar{1}010)$ face matched the four $\{11\bar{2}2\}$ traces for the $(\bar{1}010)$ surfaces as seen in Figure 11(b) and the one set observed on the $(11\bar{2}0)$ surface matched one set of $\{11\bar{2}2\}$ traces for this surface as seen in Figure 11(a). $\{10\bar{1}2\}$ type twins and basal and $(\bar{1}010)$ prism slip lines were also observed on both these surfaces.

Interferrometric studies of the rectangular extrusion markings similar to those described for specimens ISR-10, and ISR-11 and seen in Figure 12(a) and (b) for ISR-12 revealed that these regions were raised about 5000 Å above the surface, as measured by the shift in the fringes obtained with sodium yellow illumination.

Electron transmission microscopy studies of a foil cut parallel to the $(11\bar{2}0)$ surface revealed that dislocations having non-basal Burgers vectors had in fact been produced. These were seen to delineate the $(11\bar{2}2)$ traces expected for this orientation as seen in Figure 13 for the operating g.(0002) reflection. The same area examined with the g.$(10\bar{1}0)$ as the operating reflection revealed the dislocations having Burgers vectors coincident with the basal plane as well as those $(\vec{c} + \vec{a})$ vectors which were not coincident with the $(10\bar{1}0)$ plane. These studies showed that $\vec{c}$, $\vec{c} + \vec{a}$ and $\vec{a}$ Burgers vectors were present. A far greater number of dislocations having $\vec{c}$ type Burgers vectors were present in this foil suggesting that $(\vec{c} + \vec{a})$ dislocations dissociated into $\vec{c}$ and $\vec{a}$ components.

2. Zone Leveled Crystals

a. Specimen SR-11-1 (156-164 ksi Pressure)

The macroscopic photographs of this crystal after deformation under hydrostatic pressure are shown in Figure 14. The fracture occurred in the region of the platens as shown. Optical microscopy of the lateral surfaces revealed pyramidal slip only in the regions close to the platens at A and B in Figure 14 and is shown in Figure 15(a) and (b) for the $\{11\bar{2}0\}$ and $(\bar{1}010)$ surfaces. Also seen in Figure 15(a) are $\{10\bar{1}2\}$ twins and basal slip lines. The single set of pyramidal slip lines seen in Figure 15(a) matched the $\{11\bar{2}2\}$ traces expected for this surface. The slip lines observed in Figure 15(b) also matched the $(11\bar{2}2)$ traces expected for this surface.

Electron transmission microscopy studies did not reveal dislocations with non-basal Burgers vectors. Micrographs were not available at the time of this report.

Submitted by:

Nobuo Inoue
N. Inoue
Principal Scientist

V. Damiano
V. Damiano
Principal Scientist

J. E. Hanafee
J. Hanafee
Senior Research Metallurgist

G. London
G. London, Manager
Special Projects Laboratory

H. Conrad
H. Conrad, Technical Director
Materials Science and
Engineering Department

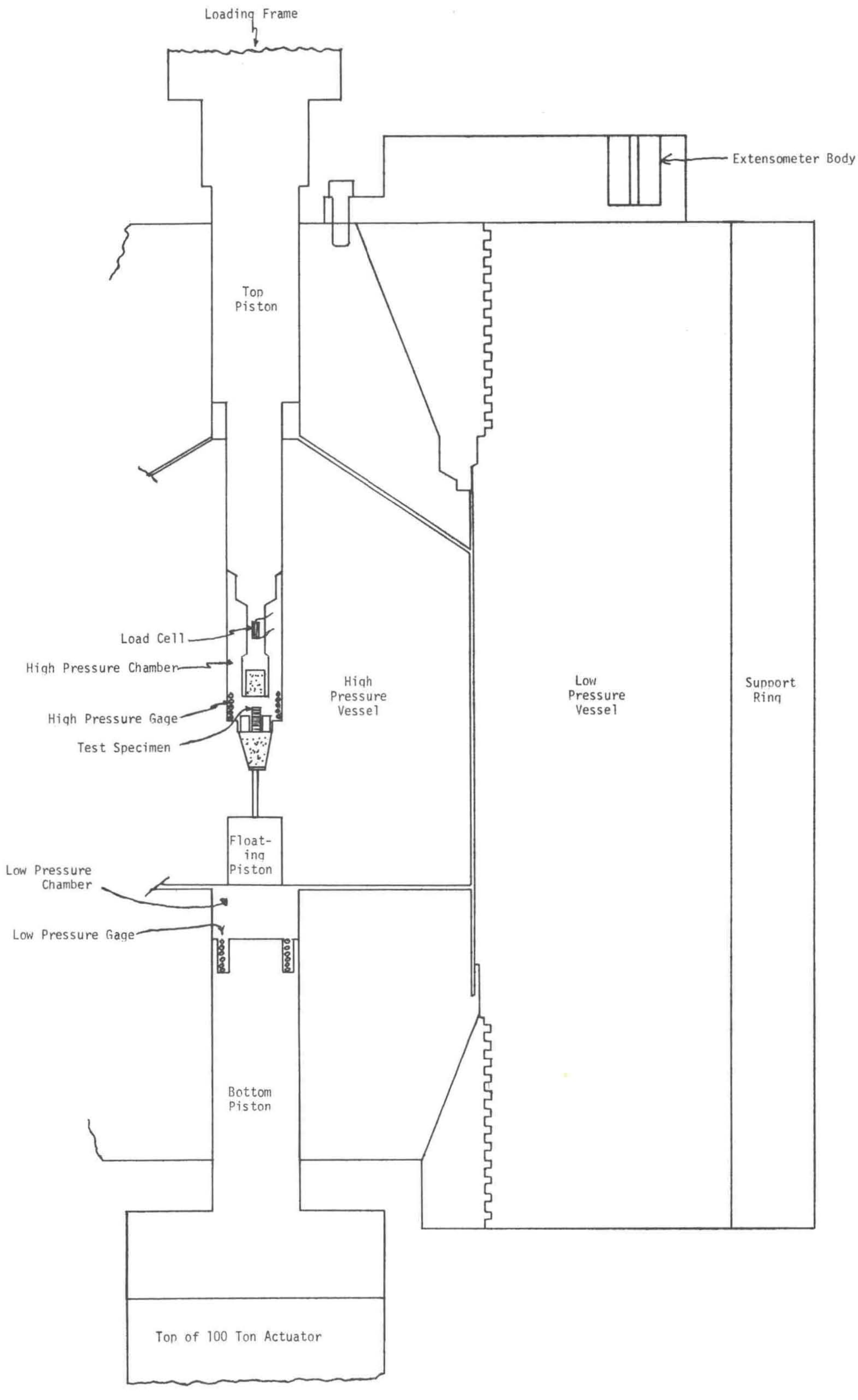

Fig. 1 - Schematic Diagram of Two-Stage High Pressure Test Vessel

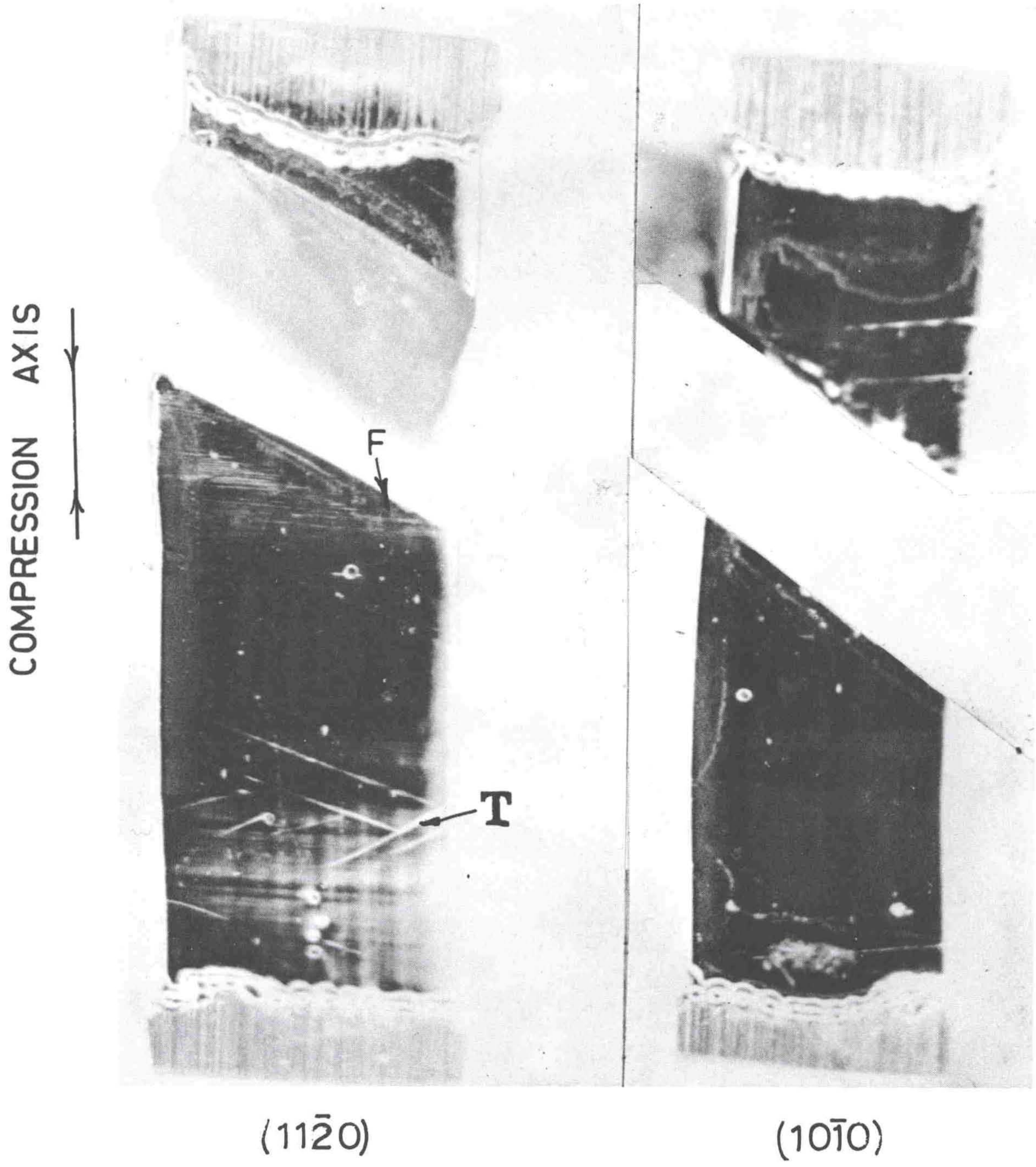

Fig. 2 - Macroscopic Photograph Showing {11$\bar{2}$0} and {10$\bar{1}$0} Lateral Surfaces of Crystal ISR-10 After c-axis Compression Under Hydrostatic Pressure in the Range 145-168 ksi. Mag. 15X

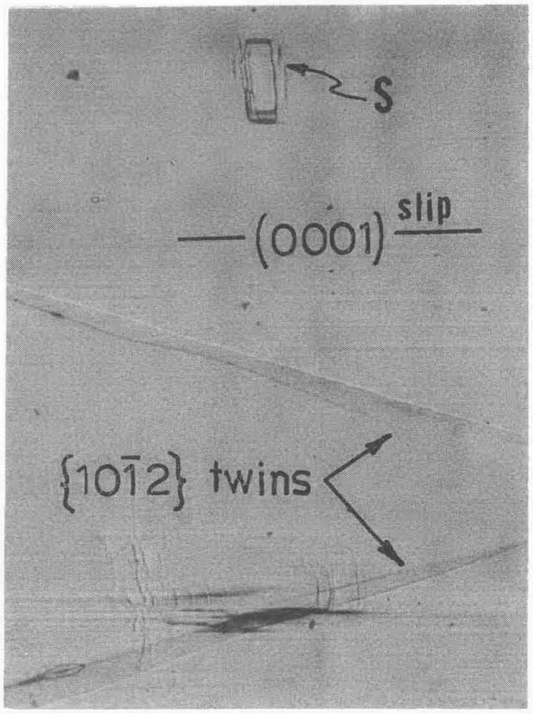

Fig. 3 - Optical Photomicrograph Showing (0001) Slip Lines, {10$\bar{1}$2} Twins and Rectangular Markings at S on (11$\bar{2}$0) Surface of Crystal ISR-10 Shown in Figure 1. Mag. 240X

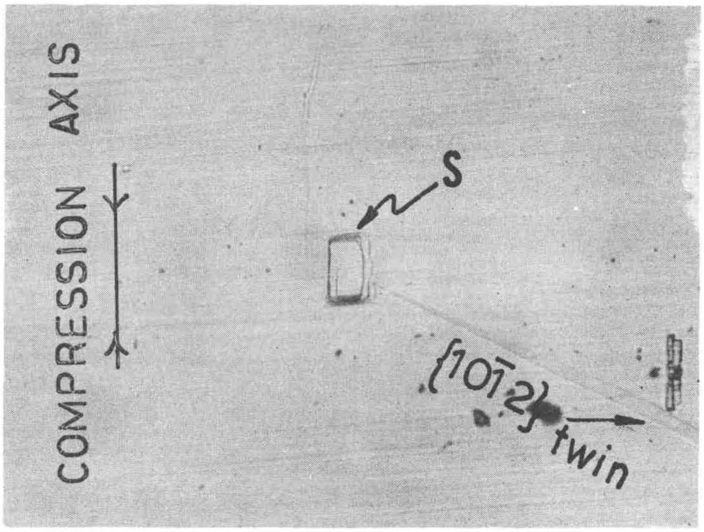

Fig. 4 - Optical Photomicrograph Showing Rectangular Marking at S at the Top of {10$\bar{1}$2} Twin of Crystal ISR-10. Mag. 240X

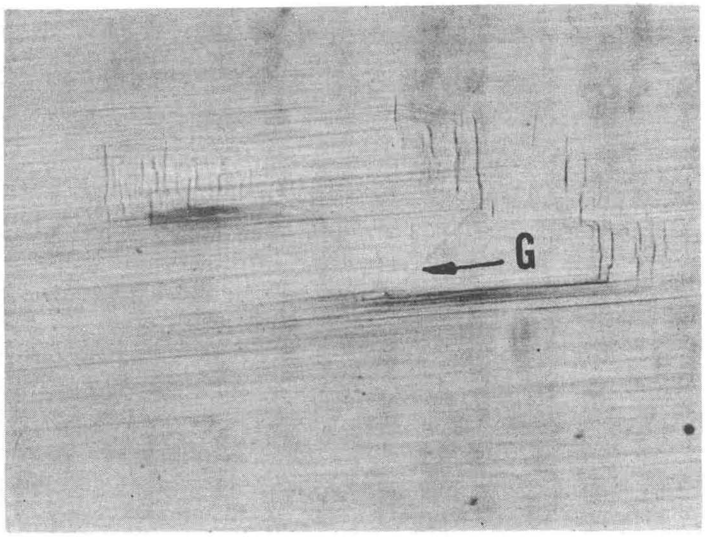

Fig. 5 - Profuse Basal and Prism Slip Seen in Association with Pyramidal Slip at G of Specimen ISR-10. Mag. 240X

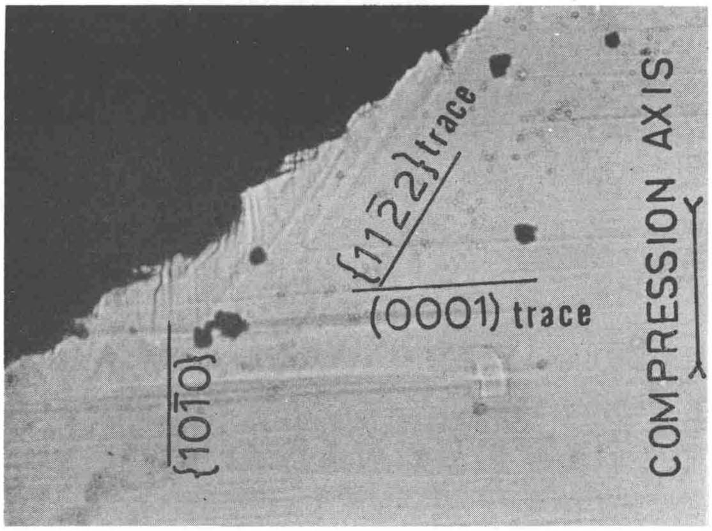

Fig. 6 - Pyramidal Slip Lines on $(11\bar{2}0)$ Surface Shown in Figure 2 at F Match $\{11\bar{2}2\}$ Trace for this Surface. Mag. 240X

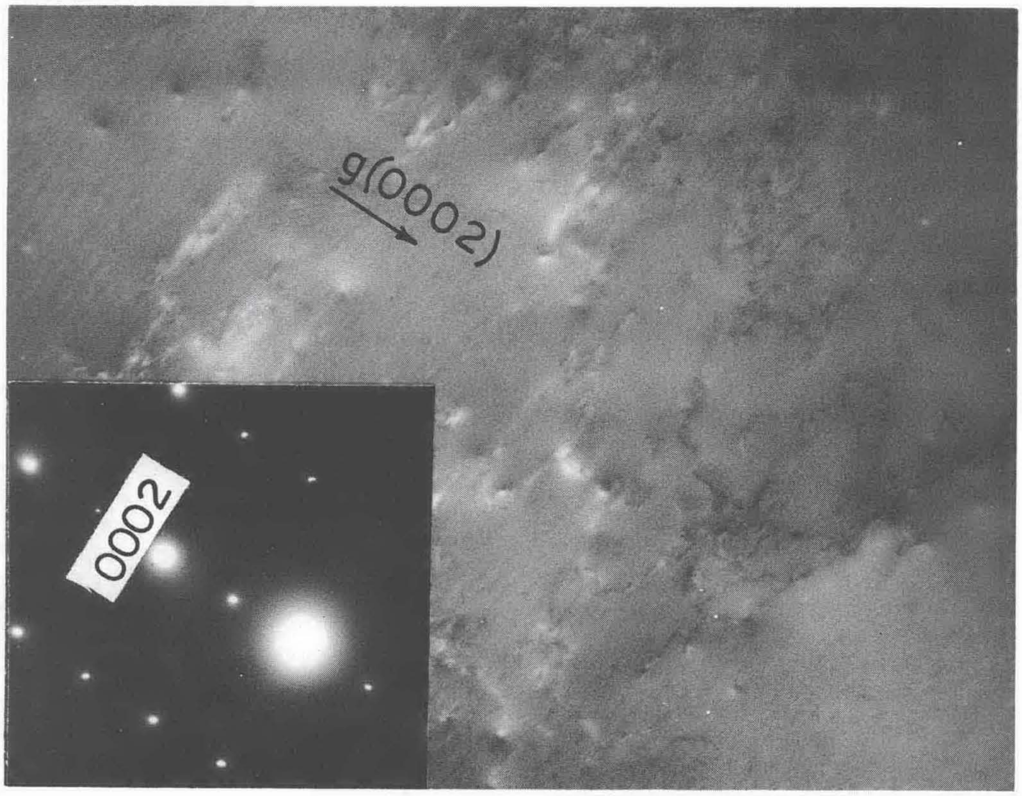

(a)

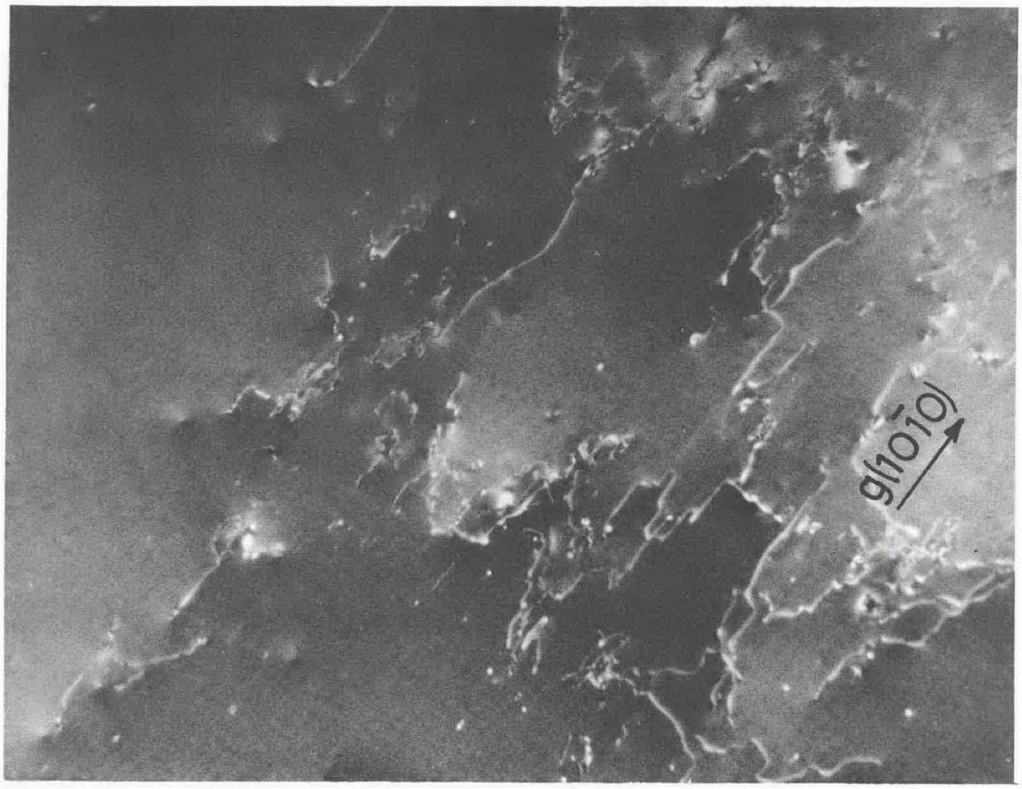

(b)

Fig. 7 - Electron Transmission Micrographs of Specimen ISR-10 Foil Cut Parallel to (11$\bar{2}$0) Showing Contrast Effects for (a) g.(0002) and (b) g.(10$\bar{1}$0). Mag. 37,500X

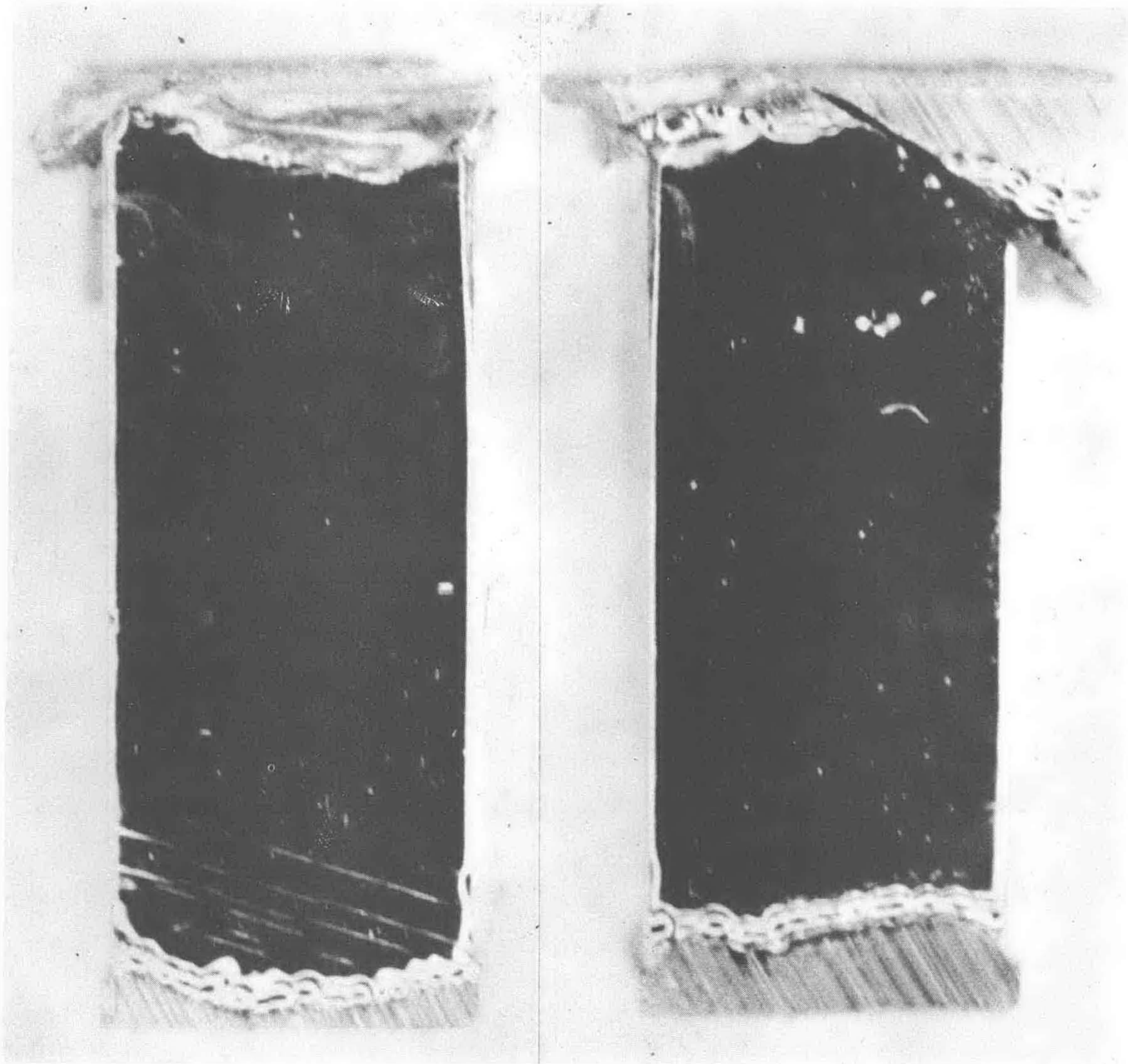

(11$\bar{2}$0) (10$\bar{1}$0)

Fig. 8 - Macroscopic Photograph Showing {11$\bar{2}$0} and {1010} Lateral Surfaces of Crystal ISR-11 After c-axis Compression under Hydrostatic Pressure in the Range 238-255 ksi. Mag. 15X

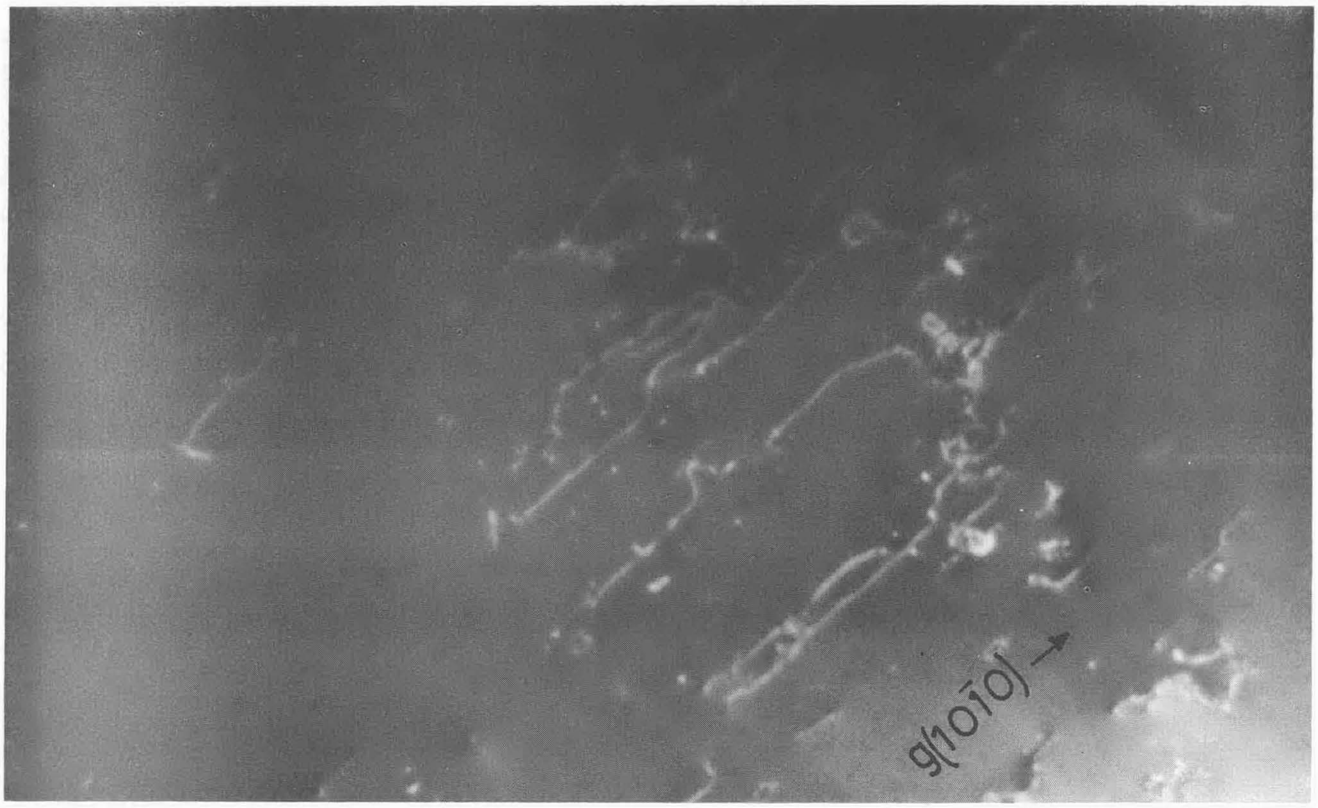

Fig. 9 - Electron Transmission Micrographs of Crystal ISR-11 Foil Cut Parallel to (11$\bar{2}$0) Showing Contrast Effects for (a) g.(0002) and (b) g.(10$\bar{1}$0). Mag. 37,500X

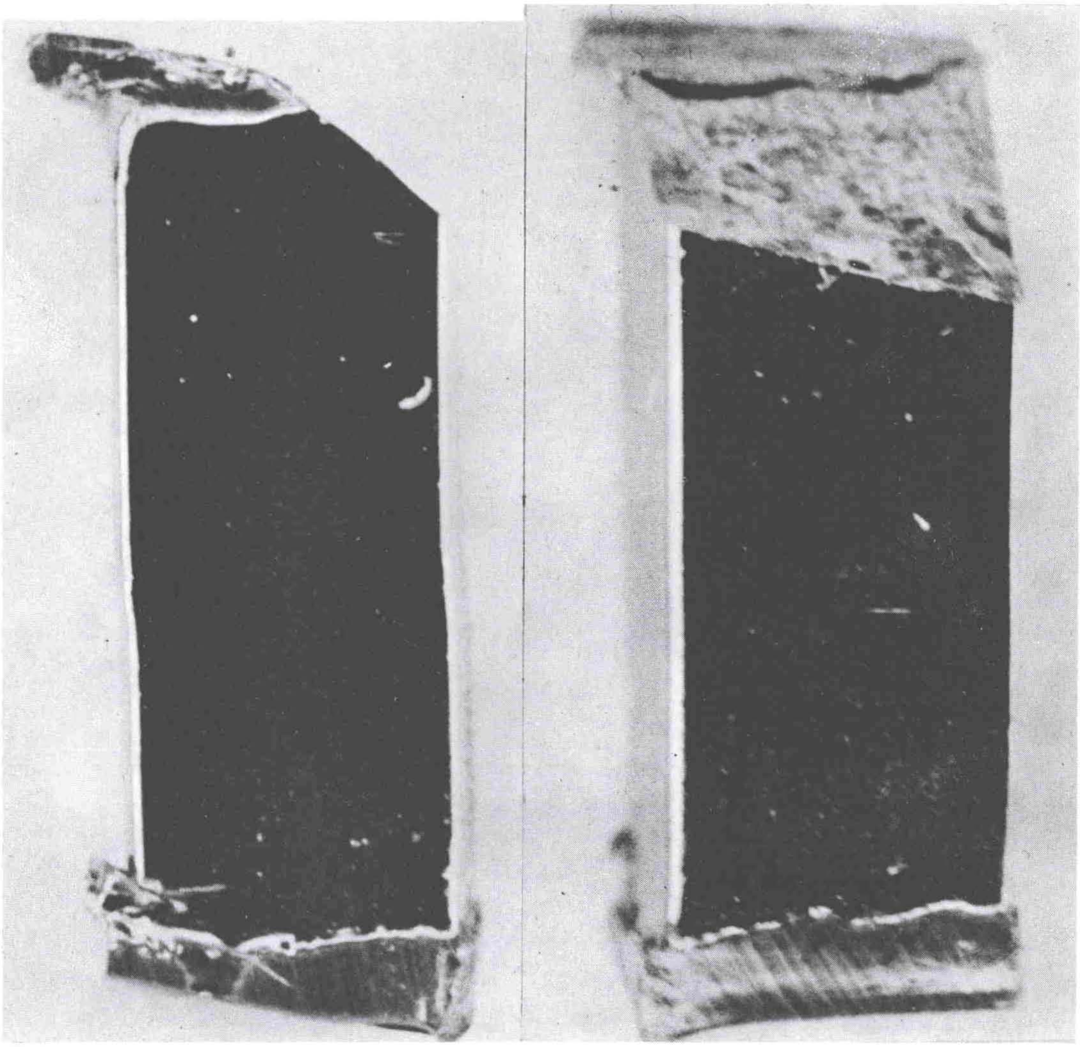

Fig. 10 - Macroscopic Photograph Showing {11$\bar{2}$0} and {10$\bar{1}$0} Lateral Surfaces of Crystal ISR-12 After c-axis Compression Under Hydrostatic Pressure in the Range 261-293 ksi. Mag. 15X

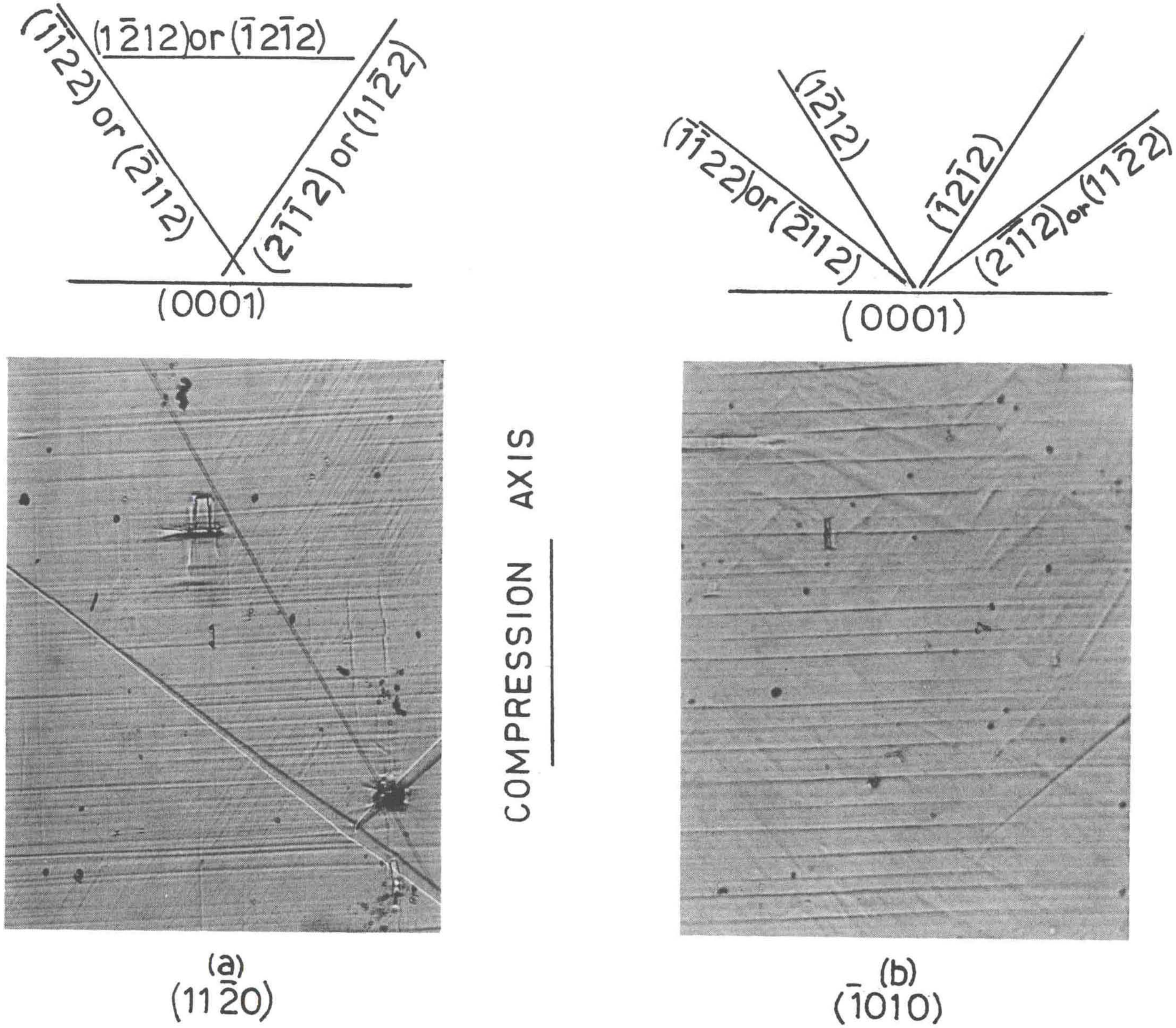

Fig. 11 - Optical Photomicrographs of (a) (11$\bar{2}$0) and (b) ($\bar{1}$010) Surfaces of Crystal ISR-12 Showing Pyramidal Slip Lines which are Indexed as {1122} Traces. Mag. 240X

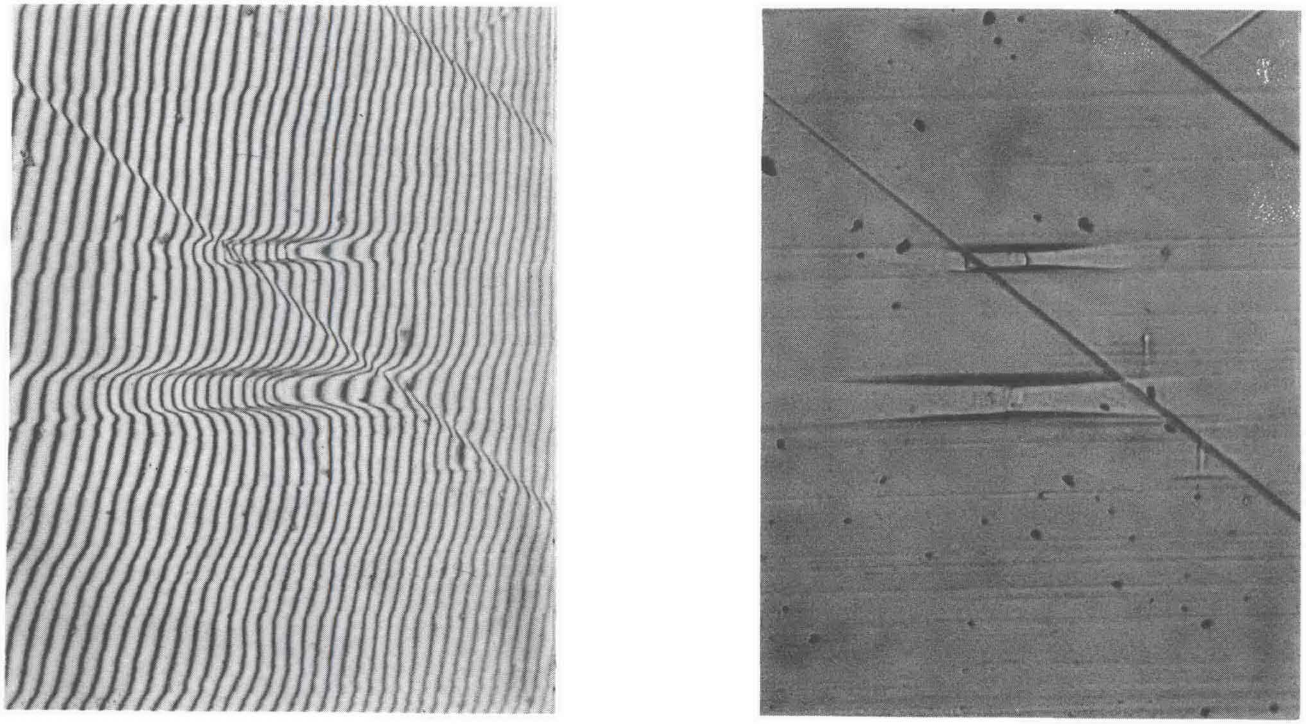

(a) (b)

Fig. 12 - Optical Photomicrograph of Crystal ISR-12 Showing Interference Fringes on Rectangular Markings of Lateral (11$\bar{2}$0) Surface (a) with fringes, (b) without fringes. Mag. 260X

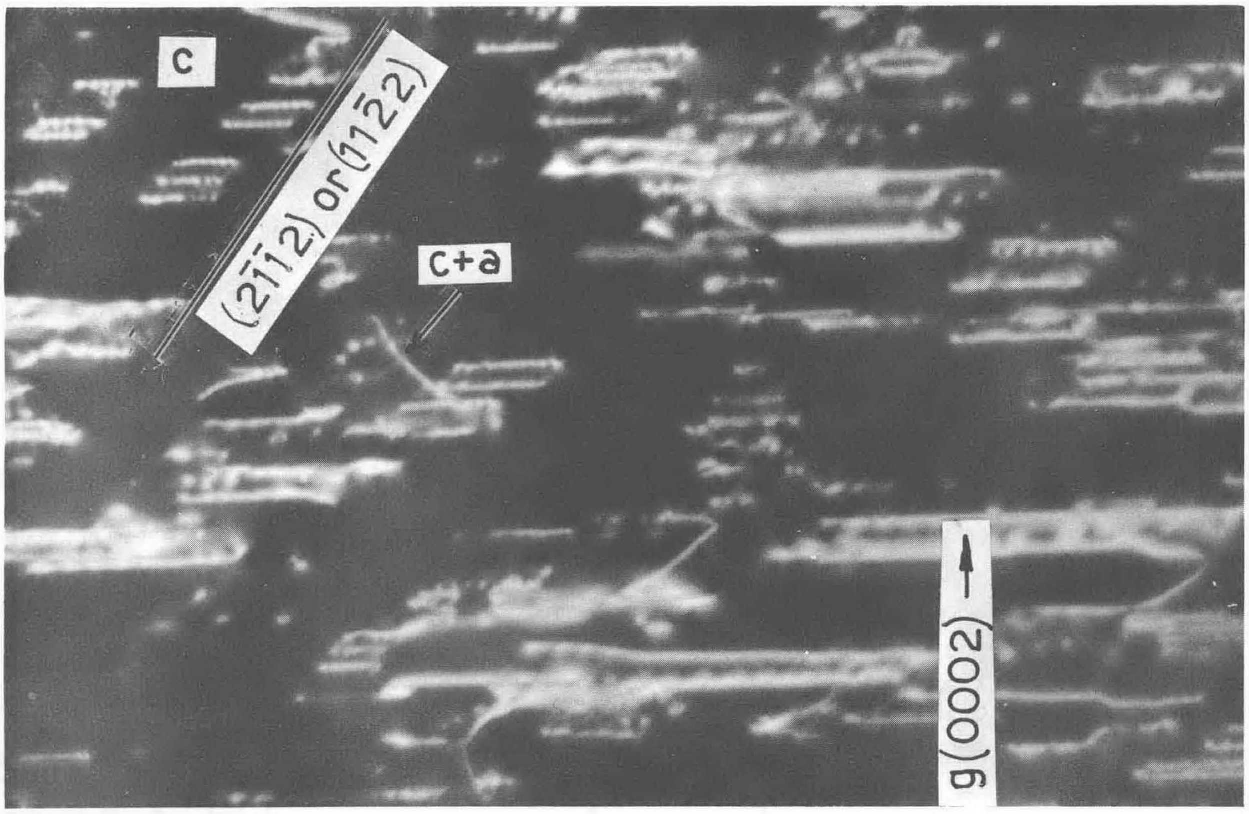

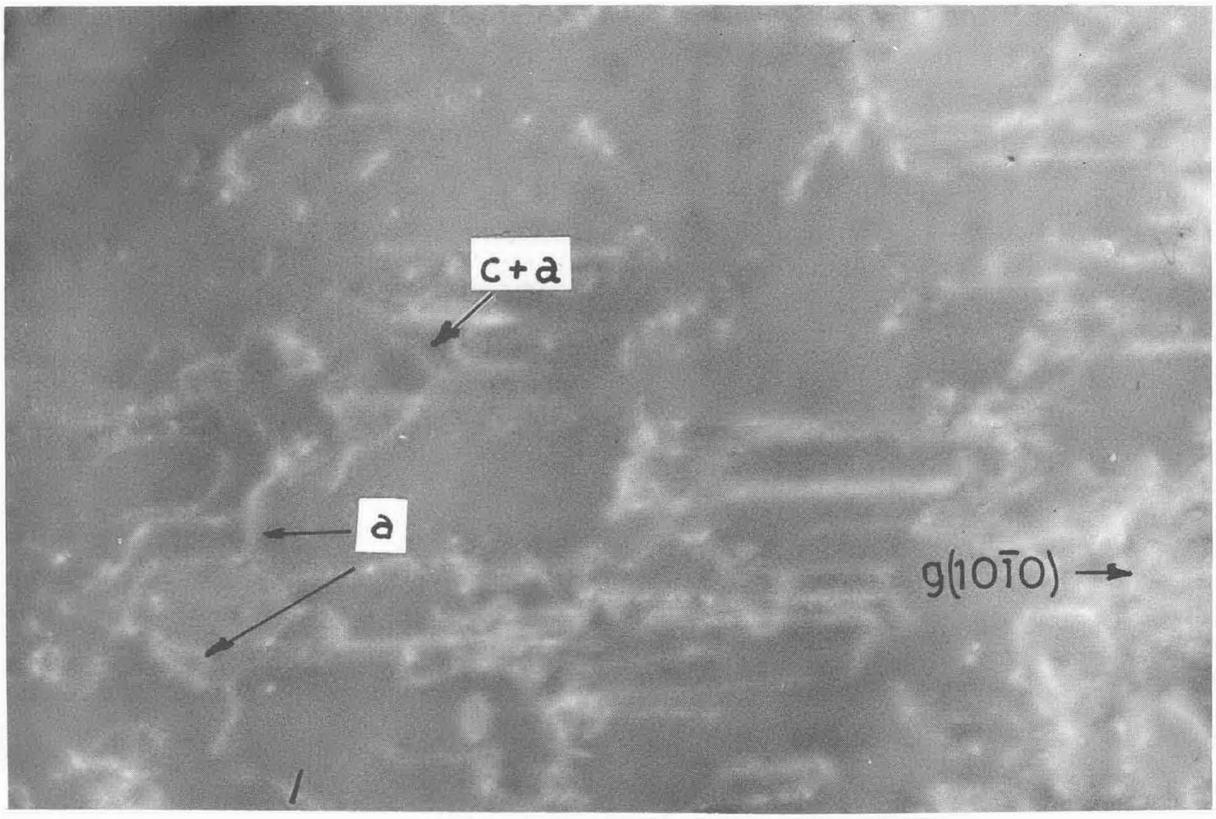

Fig. 13 - Electron Transmission Micrographs of Crystal ISR-12 Foil Showing Diffraction Contrast in Foil Cut Parallel to (11$\bar{2}$0) for (a) g.(0002) and (b) g.(10$\bar{1}$0) - Pyramidal Slip Lines are Delineated by Dislocations Having non-basal Burgers vectors. Mag. 37,500X

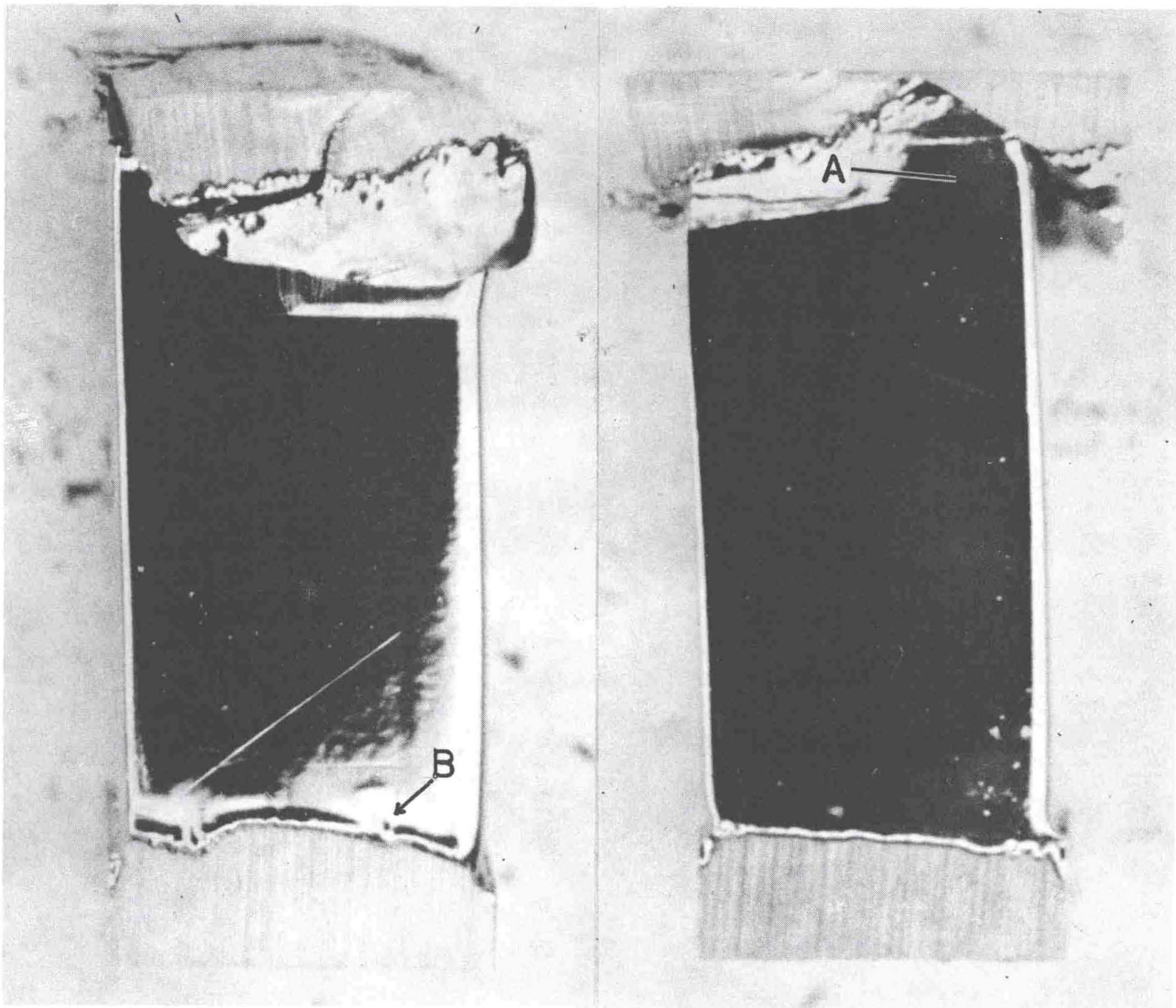

Fig. 14 - Macrophotograph Showing {11$\bar{2}$0} and {$\bar{1}$010} Lateral Surfaces of Crystal SR-11-1 After c-axis Compression Under Hydrostatic Pressure in the Range 156-164 ksi.

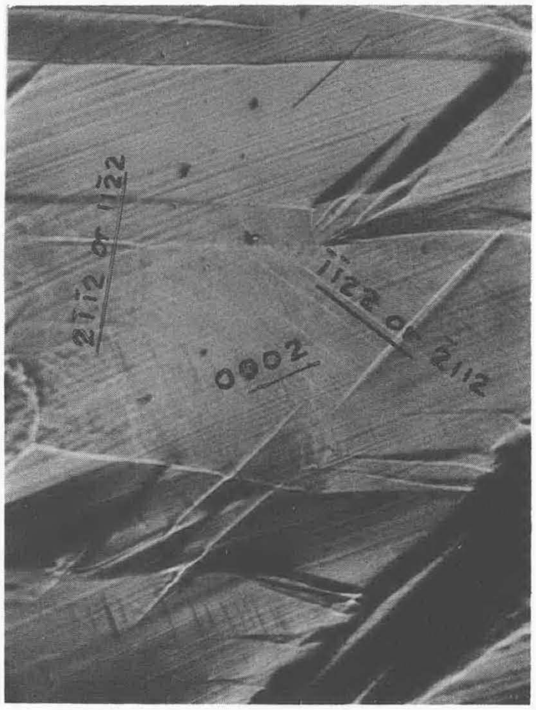

(a)

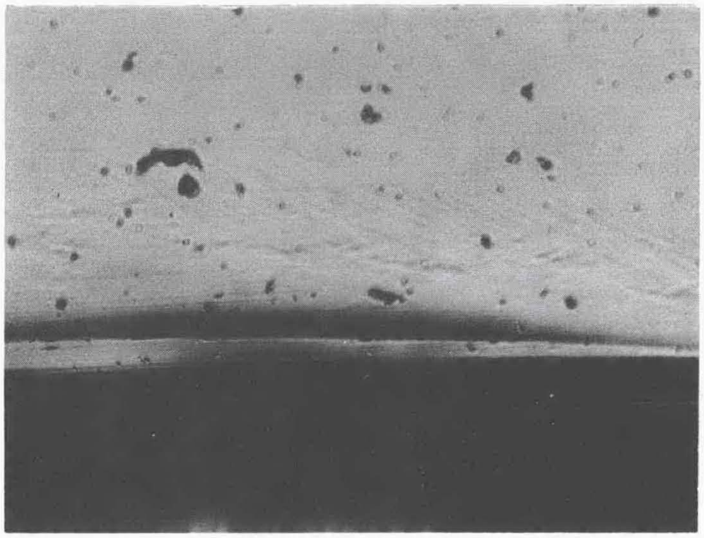

(b)

Fig. 15 - Optical Photomicrograph of (a) ($11\bar{2}0$) Surface and (b) ($10\bar{1}0$) Surface of Crystal SR-11-1 Showing Pyramidal Slip Lines. Mag. 240X